Wireless optoelectronic devices for vagus nerve stimulation in mice

Donahue, Mary J; Ejneby, Malin Silverå; Jakešová, Marie; Caravaca, April S; Andersson, Gabriel; Sahalianov, Ihor; Đerek, Vedran; Hult, Henrik; Olofsson, Peder S; Głowacki, Eric Daniel

Journal of Neural Engineering

PAPER

Wireless optoelectronic devices for vagus nerve stimulation in mice

Mary J Donahue[1,9], Malin Silverå Ejneby[1,2,9], Marie Jakešová[3,9] ⬤, April S Caravaca[4,5], Gabriel Andersson[6], Ihor Sahalianov[3] ⬤, Vedran Đerek[7], Henrik Hult[5,6], Peder S Olofsson[4,5,8] ⬤ and Eric Daniel Głowacki[1,3,*] ⬤

1 Laboratory of Organic Electronics, Campus Norrköping, Linköping University, SE-60174 Norrköping, Sweden
2 Wallenberg Centre for Molecular Medicine, Linköping University, SE-58185 Linköping, Sweden
3 Bioelectronics Materials and Devices Laboratory, Central European Institute of Technology, Brno University of Technology, Purkyňova 123, 61200 Brno, Czech Republic
4 Laboratory of Immunobiology, Center for Bioelectronic Medicine, Department of Medicine, Center for Molecular Medicine, Karolinska Institutet, Stockholm, Sweden
5 Stockholm Center for Bioelectronic Medicine, MedTechLabs, Karolinska University Hospital, Solna, Sweden
6 Department of Mathematics, KTH, 11428 Stockholm, Sweden
7 Department of Physics, Faculty of Science, University of Zagreb, Bijenička c. 32, 10000 Zagreb, Croatia
8 Institute of Bioelectronic Medicine, Feinstein Institutes for Medical Research, Manhasset, NY, United States of America
9 These authors contributed equally to this work
* Author to whom any correspondence should be addressed.

E-mail: Eric.Daniel.Glowacki@ceitec.vutbr.cz

Abstract

Objective. Vagus nerve stimulation (VNS) is a promising approach for the treatment of a wide variety of debilitating conditions, including autoimmune diseases and intractable epilepsy. Much remains to be learned about the molecular mechanisms involved in vagus nerve regulation of organ function. Despite an abundance of well-characterized rodent models of common chronic diseases, currently available technologies are rarely suitable for the required long-term experiments in freely moving animals, particularly experimental mice. Due to challenging anatomical limitations, many relevant experiments require miniaturized, less invasive, and wireless devices for precise stimulation of the vagus nerve and other peripheral nerves of interest. Our objective is to outline possible solutions to this problem by using nongenetic light-based stimulation. *Approach.* We describe how to design and benchmark new microstimulation devices that are based on transcutaneous photovoltaic stimulation. The approach is to use wired multielectrode cuffs to test different stimulation patterns, and then build photovoltaic stimulators to generate the most optimal patterns. We validate stimulation through heart rate analysis. *Main results.* A range of different stimulation geometries are explored with large differences in performance. Two types of photovoltaic devices are fabricated to deliver stimulation: photocapacitors and photovoltaic flags. The former is simple and more compact, but has limited efficiency. The photovoltaic flag approach is more elaborate, but highly efficient. Both can be used for wireless actuation of the vagus nerve using light impulses. *Significance.* These approaches can enable studies in small animals that were previously challenging, such as long-term *in vivo* studies for mapping functional vagus nerve innervation. This new knowledge may have potential to support clinical translation of VNS for treatment of select inflammatory and neurologic diseases.

1. Introduction

Many of the most debilitating and deadly diseases, including cancer, cardiovascular diseases, and autoimmune diseases, develop over a long time, making it difficult to study the mechanisms of disease pathogenesis in acute animal models. Anatomical and functional mapping of neural reflexes is required to

delineate the role of nerve signals in the pathogenesis for a wide range of common diseases [1–4]. Recent work has opened new potential therapeutic avenues [5], however, the available methods to study the effects of selective peripheral nerve activation in animal models often employ bulky devices, consisting of rudimentary electrodes, wires, and power sources [6–8]. Long-term experiments under relatively normal living conditions are very difficult or impossible to perform. This is a particular challenge for smaller laboratory animals [6, 7, 9, 10], such as the mouse, which is a well-established model organism for the study of many disease mechanisms [11].

The right and left vagus nerve innervate many inner organs in the thorax and abdomen [2]. Vagus nerve stimulation (VNS) is clinically used to treat patients with drug-resistant epilepsy [12, 13], depression [14], and cluster headaches [15]. VNS is also investigated, in clinical trials, for numerous other applications, such as treatment of inflammatory diseases [16–19], cardiovascular diseases [2], and neurological diseases and disorders [20, 21]. Long-term VNS studies have mainly been carried out in larger animals [7, 22, 23], while experimental work on mice has primarily been limited to acute studies [6, 24–32], and only two recent studies have addressed long-term VNS in mice [7, 33]. It is therefore evident that progress in electrode design and miniaturization is still needed for stimulating small diameter peripheral nerves beyond acute studies.

Recent developments in flexible substrates, stable electrode materials, and miniaturization of devices for accessing, recording, and stimulating the central and peripheral nervous systems, as well as various organs, are providing an increasingly useful set of experimental tools [34–38]. Emerging wireless technologies, relying on radio frequency power transmission or electromagnetic induction [39], ultrasound [40, 41], or light [42–46], have the potential to allow for chronic interfacing with peripheral nerves, however they still lack the size scalability necessary to stimulate small diameter nerves. Most miniaturized implantable systems for interfacing with the peripheral nervous system are tested in small mammals such as rats and target larger diameter nerves such as the sciatic nerve [46–49]. In general, the cervical vagus nerve has a much smaller diameter than the sciatic nerve, with a size difference in rats of approximately a factor of $2.5\times$ [50]. Furthermore, the diameter of the cervical vagus nerve in mice is approximately 180 μm, compared to that of rats which is about 260 μm [51, 52]. Nerve cuff electrodes for rats and mice therefore have different size requirements [10], and access to suitable electrode interfacing devices is required in order to properly target specific anatomical structures.

In this work we have designed and explored the use of a flexible wired multi-electrode array (figure 1(A)), and two wireless organic photovoltaic electrodes which convert deep-red light into electrical currents (figures 1(B) and (C)), for activating the right cervical vagus nerve of mice. The right vagus nerve innervates the sinoatrial node and reduces the heart rate (HR) upon electrical activation [30, 53]. In our experiments the use of this HR variation was chosen as a read-out as it is straightforward to track in real time. The HR is lowered through the recruitment of medium-sized B fibers within the vagus nerve [54, 55]. The composition of fiber types is similar between species [52], however, the mice vagus nerves contain only one fascicle, in contrast to humans or larger animals which have multiple fascicles and more fibrous tissue [52]. These differences affect the stimulation parameters used between species. Our flexible wired multi-electrode array enabled systematic testing of different stimulation parameters and electrode layouts for optimal activation of the right cervical vagus nerve in mice. These results, in combination with finite element simulations, were used to design wireless organic photovoltaic electrodes that can be actuated from outside of the body with deep-red light (638 nm). This builds on our previous work with organic electrolytic photocapacitor (OEPC) devices (figure 1(B)) for stimulating neuronal tissues such as large (1 mm Ø) peripheral nerve or the cortical surface [43–46]. Extrapolating the photocapacitive stimulation concept to the much smaller mouse vagus nerve is not straightforward and we report that it is difficult to implement to practically stimulate this nerve. To overcome this issue, we show how a 'photovoltaic flag' device (figure 1(C)), robustly activates the vagus nerve in mice, also when actuated using light transmitted through tissue. This is a result of a higher amount of photogenerated charge at the larger PN heterojunction of the 'flag', which can be efficiently concentrated to the nerve through the use of microelectrodes (see figure 1). We have engineered these devices to deliver the same charge densities to the nerve as the optimized wired arrays. Thus, photovoltaic flags have the potential to enable implementation of wireless electrical stimulation for small diameter peripheral nerves.

2. Methods

2.1. Animals
Male C57BL/6 J mice from Charles River Laboratories (age 10–16 weeks) were used. Mice were housed in a laboratory environment on a 12 h light/dark cycle, with ad libitum access to food and water.

2.2. Vagus nerve isolation
The cervical vagus nerve isolation method used here has been previously described [6]. Briefly, anesthesia was induced using isoflurane at 3% in a 1:1 mixture of oxygen and air. Following induction of anesthesia, mice were placed on the surgical mat in the

Figure 1. Optimization process flow for microfabricated stimulators of the right vagus nerve. (A) Wired electrode array for controlled stimulation parameters and electrode layouts. The eight stimulation electrodes consist of Au contacts, coated with PEDOT:PSS and have dimensions of 200 μm $\times$ 450 μm, while the smaller electrodes (not used in this study) are 200 μm $\times$ 30 μm. The utilized dimensions allow the electrodes to fully wrap around the right vagus nerve of mice. (B) An ultrathin, wireless, OEPC device, previously shown to stimulate neuronal tissues including the rat sciatic nerve [46]. The PN heterojunction pixel is marked 'C' as negative charge accumulates at the nerve interface upon illumination with deep-red light (638 nm), providing the cathodic (C) stimulation pulse. The PN pixel diameter is 1 or 1.4 mm in this study, while the remaining area, marked as 'A', represents the transparent Au return electrode which gives the anodic (A) charge balancing pulse. (C) Photovoltaic flag device with the indicated light absorbing 'flag' consisting of two photovoltaic cells in series, each with dimensions of 1.8 mm $\times$ 3 mm. Encapsulated Au leads connect the flag to the stimulation electrodes, which conformally wrap around the right vagus nerve of mice. For all three devices a parylene C (PaC) handling flap is used to assist the implantation.

supine position, and maintained at 1.0%–1.25% isoflurane in a 1:1 oxygen:air mixture. A ventral midline cervical incision was made between the mandible and sternum and subcutaneous tissues were separated to expose the salivary glands which were separated to reveal the sternomastoid and sternohyoid muscles along the trachea. Separation of tissues revealed the common carotid artery and the cervical vagus nerve. The vagus nerve was isolated away from the carotid artery and the surrounding connective sheath tissue. A piece of polypropylene suture was placed under the vagus nerve to facilitate placement of the electrode. The parylene C (PaC) handling flaps (see figure 1) of the stimulation device to be used were then manipulated with forceps to pull it under the nerve. Once the electrodes were properly placed, the device was wrapped around the nerve and the PaC surfaces were laminated onto each other having sufficient adhesion for the acute experiments.

2.3. Stimulation array fabrication and electrical stimulation

A flexible electrode array was designed to provide both stimulation and recording capability. This array consists of seven smaller contact surfaces (recording, not utilized in this study) and eight larger contact surfaces (stimulation), the latter each possess dimensions of 450 μm $\times$ 200 μm. The stimulation electrodes are produced in a 2 $\times$ 4 arrangement, providing the possibility to test a variety of electrode stimulation layouts. Overall, the device was created through microfabrication techniques previously described [56] to create a cuff-like layout that can conform closely around the nerve. Briefly, a 2 μm thick, ultra-flexible PaC substrate is deposited by chemical vapor deposition (CVD) (Diener electronic GmbH) on glass microscope slides cleaned by ultrasonication first in 2% Hellmanex in deionized water (DIW), followed by acetone, and then isopropanol.

Subsequently, 80 nm thick gold interconnects with a 5 nm titanium adhesion layer are photolithographically patterned using the negative photoresist AZ nLof 2070, a MA6 Suss mask aligner with i-line filter, and AZ 326 MIF developer. These contact lines allow electrical connection and wiring possibility upon completion. A 2 min O_2 plasma process is carried out (50 W) followed by deposition of a 1.5 μm thick insulating PaC layer over the metal lines using a silane adhesion promoter, A-174. To define the outline shape of the probes, a photoresist etch mask (AZ 10XT) is patterned and a reactive ion etching (RIE) step with O_2/CF_4 (150 W) is performed. Afterward, the etch mask is removed with an acetone wash and isopropanol rinse and a dilute (2.5 vol% in DIW) soap anti-adhesion layer is spin coated (1000 rpm) onto the surface. Next, a 2 μm thick sacrificial PaC layer is deposited. Afterward an AZ 10XT photoresist etch mask is used once again with the RIE process to define the electrode surface and to provide back-end contact possibility. A poly(3,4-ethylenedioxythiophene):polystyrene sulfonate (PEDOT:PSS) coating is utilized at the electrode sites to reduce electrochemical impedance and to improve recording and stimulation performance. This coating is a dispersion of PEDOT:PSS (Clevios^{TM} PH 1000 from Heraeus Holding GmbH), 5 wt% ethylene glycol (EG), 0.1 wt% dodecyl benzene sulfonic acid, and 1 wt% of (3-glycidyloxypropyl)-trimethoxysilane (GOPS), which was spin coated onto the substrates. The sacrificial PaC layer is removed through a peel-off technique and the samples are annealed at 140 C for 45 min to crosslink the film. DIW is used to assist in the removal of the completed probes from the glass substrates.

Stimulation was performed using the Intan RHS 128-channel stimulation/recording controller and software (Intan Technologies, CA, USA). Zero insertion force clips (ZIF-clip) were used to connect directly to the wired electrode arrays. A custom-made printed circuit board adapter provided connection between the ZIF clip and the Intan 16-channel headstage. Data acquisition was carried out and stimulation parameters were set within the INTAN software. For a given stimulation pulse, the charge density per phase (D) was calculated as follows:

$$D = \frac{(I \times \text{PD})}{A} \qquad (1)$$

where I is the current magnitude, PD is the pulse duration in seconds, and A is the area of the electrode. The values given here are converted to μC/cm^2/phase.

The total charge injected per phase (C) was then calculated as follows:

$$C = (I \times \text{PD}) \times N_E \qquad (2)$$

where I is the current magnitude, PD is the pulse duration in seconds, N_E is the total number of electrodes

in the configuration used. Values here are given in μC/phase.

Electrochemical characterization of the stimulation electrodes was carried out with an Ivium technologies Vertex One potentiostat. Electrochemical impedance spectroscopy was measured in the frequency range of 250 kHz–1 Hz for electrodes with gold surfaces as well as with PEDOT:PSS coatings. Voltage transients were measured for current pulses utilized in this study (up to 20 μA for 266 μs pulse duration and up to 5 μA for 1 ms duration, $n = 6$ from two devices (mean $\pm$ SD)).

2.4. OEPC device fabrication and light-induced stimulation

Fabrication of OEPC devices was carried out as previously described [46]. Briefly, glass microscope slides were cleaned in acetone, isopropanol, and a 2% Hellmanex in DIW solution. The glass surface was treated with oxygen plasma (200 W, 600 s, Diener electronic GmbH) and a flexible (2 μm thick) PaC substrate layer was deposited. Subsequently, the semi-transparent bottom electrode was deposited in a sputtering system. It consisted of 1 nm Pd as a sticking layer, 9 nm of Au, and a 30 nm indium tin oxide (ITO) as a protective layer. The full device area was patterned using a photoresist mask (S1818, MF-319 developer), wet etching (conc. HCl for ITO, KI/I_2 mixture for Au and Pd) and a RIE process. The bottom electrode area was defined by a photoresist mask (S1818) and wet etching. After photoresist removal, a sacrificial PaC layer was used to pattern the organic PN heterojunction through a peel-off process. An anti-adhesion layer was first spin coated onto the substrates (2% Micro 90 soap in DIW, $\leqslant$1000 rpm, no baking step) and a 2.5 μm layer of PaC was deposited. The PN pixel areas were defined using an etch mask (AZ 10XT), RIE process to remove the sacrificial parylene areas, and an HCl wet etch to remove the protective layer of ITO. The PN junction consists of metal free phthalocyanine (H_2Pc, P-type, 30 nm) and *N,N'*-dimethyl perylenetetracarboxylic bisimide (PTCDI, N-type, 30 nm) which were purified by threefold temperature-gradient sublimation. These PN layers were thermally evaporated from resistively heated crucibles ($<1 \times 10^{-6}$ Torr, rates of 1–6 Å s^{-1}) and the sacrificial PaC layer was peeled to remove superfluous material, leaving behind the desired pixels. In the cases where a PEDOT:PSS coating was used to enhance OEPC performance, PEDOT:PSS mixture (Clevios^{TM} PH 1000, 1 wt% dimethyl sulfoxide, and 2 wt% GOPS) was spin coated at 5000 rpm for 1 min and dried at 90 °C for 45 s before peeling off the sacrificial PaC layer. The devices were then annealed at 120 °C for 1 h. Following completion of the fabrication process, DIW is used to assist in the removal of the OEPC devices from the glass substrates.

Light absorption occurs in the H_2Pc layer and negative charges generated ($-$) accumulate at the PTCDI electrolytic interface while the thin, semi-transparent Au layer capped by ITO acts as the return ($+$) electrode [43, 45]. Pulsed deep-red light is thus converted to charge-balanced biphasic electrical signals by the OEPC device. A 638 nm laser diode with a maximal output power of 700 mW, controlled by a ThorLabs DC2200 high-power LED driver, was used for activating the OEPC device, wrapped around the nerve with the charge generating PN heterojunction (photoelectrode) and Au return electrode facing the nerve interface. Light intensity was verified and measured with a Thorlabs Si PIN diode (Thorlabs SM1PD1B).

2.5. Photovoltaic flag device fabrication and light-induced stimulation

Glass microscope slides were cleaned, and a flexible (2 μm thick) PaC substrate was deposited by CVD (same conditions as the OEPC protocol above). To create the conductive leads between the photovoltaic flag pixels and the stimulation electrodes, 3 nm Pd and 80 nm Au layers were deposited via thermal evaporation (vacuum $< 2 \times 10^{-6}$ Torr, deposition rate 2–5 Å s^{-1}) and patterned using a positive photoresist (S1818 and MF-319 developer) and a subsequent KI/I$_2$ wet etchant to remove both metal layers. Afterward, the remaining photoresist was stripped, and the 10 nm Au PV bottom electrode was then patterned by thermal evaporation and lift-off (AZ nLOF 2070 photoresist). Subsequently, the same organic PN layer materials were used as in the OEPC devices. In the PV case, the heterojunction was formed by 40 nm of H_2Pc and 50 nm of PTCDI deposited through a shadow mask. The PV top electrode was made up of a 50 nm Ti layer, thermally evaporated through a shadow mask ($<1 \times 10^{-6}$ Torr, at a rate of 15 Å s^{-1}). The samples were encapsulated with a 2 μm PaC layer, deposited with 3-(trimethoxysilyl)propyl methacrylate (A-174) present in the CVD chamber as an adhesion promoter. The device outline was patterned by RIE using an AZ 10XT photoresist etch mask (as above). The residual resist was washed with acetone and the samples were quickly rinsed with isopropanol and DIW. A 2.5 μm sacrificial PaC layer was used to pattern the stimulation electrodes intended to be in contact with the nerve. Before the PaC deposition, an anti-adhesive layer (2% Micro 90 soap in DIW) was spin coated onto the substrates ($\leqslant$1000 rpm, no baking step). The electrode openings were patterned once again by the RIE process with AZ 10XT photoresist etch mask. The residual resist was removed with an acetone wash, followed by a quick isopropanol and DIW rinse. Immediately after etching and cleaning, a solution containing PEDOT:PSS (PH1000, Heraeus GmbH), 5 wt% EG, 0.1 wt% 4-dodecylbenzenesulfonic acid and 1 wt% GOPS was freshly prepared and spin coated in three layers (3000, 750, and 750 rpm) with a 45 s bake at 90 °C after each layer (substrate cooling was allowed between coatings). After the final layer, the sacrificial PaC layer was peeled off yielding the microelectrodes. The devices were finally annealed at 90 °C for 2 h and then washed in DIW to remove the residual soap and other chemicals. The photovoltaic part was composed of two PV cells (each 4.2 mm^2 active area) connected in series, while the PEDOT:PSS electrodes were 400 μm $\times$ 450 μm. A 638 nm laser diode with a maximal output power of 700 mW was used for activating the photovoltaic flag, as described for the OEPC devices above.

2.6. Simulation of electric fields in nerve segment

Simulation of electric fields in a nerve segment was conducted with the finite element method, implemented in the COMSOL 5.0 software package [57]. The model geometry consisted of a nerve segment wrapped by an electrode array (longitudinal layout; figures 4(C1) and S2(A)) and grounded on the sides to create realistic boundary conditions. The nerve segment was modeled as a cylinder with a diameter of 160 μm (figures 4(C) and S2(B)) and represented by three domains: nerve endoneurium with anisotropic conductivity, epineurium shell, and an outer saline layer (30 μm). Conductivity and dielectric permittivity were adopted from Bucksot *et al* [50] and can be found in table S3. The description and sizes of the electrode wrapping can be found in figure S2(A).

Electric fields were calculated by solving quasi-stationary equations, implemented in the ACDC module of COMSOL and used in similar simulations [43, 50, 58]

$$\nabla \cdot \mathbf{J} = Q_j \tag{3}$$

$$\mathbf{J} = \sigma \mathbf{E} \tag{4}$$

$$\mathbf{E} = -\nabla V \tag{5}$$

$$\mathbf{D} = \varepsilon_0 \varepsilon_r \mathbf{E} \tag{6}$$

where $\mathbf{J}$ is current density, $\mathbf{E}$ is an electric field, $\mathbf{D}$ is a displacement vector, V is potential, ε_r is the dielectric permittivity of a nerve segment and Q_j are current sources.

The system was grounded on both sides of nerve tissue using boundary condition $V = 0$. A current of -20 μA (or 20 μA) was applied to the surface of each electrode in the array. The computational mesh was assembled from tetrahedral elements with a maximum element size of 0.01 mm, and a minimum size of 2 μm and consisted of approximately 3.5 million domain elements.

2.7. HR monitoring and analysis

The HR was continuously monitored at a sampling rate of 15 Hz (Windaq Waveform file), using a pulse oximeter with a thigh sensor (MouseOx® STARR Life Sciences, MA, USA, figure 3(A)). Mice were allowed to recover from deep anesthesia, and the nerve from the handling, for around 5–10 min before the electrode simulation started. The stimulation-induced HR change was calculated as the percentage difference in mean HR_0 (i.e. mean HR 10 s pre-stimulation), and mean HR_{stim} (i.e. mean HR of a 10 s interval during stimulation, where the 10 s subinterval with the lowest mean HR is selected from the 20 s stimulation time interval).

The HR reduction was considered significant if the response $(R) < -2$ standard deviations, as following:

$$R = (HR_{stim} - HR_0)/\max(\sigma_0, \sigma_{min}) \qquad (7)$$

where HR_0 and σ_0 are the mean HR and standard deviation pre-stimulation. HR_{stim} is the mean during stimulation where the largest effect from stimulation is observed (as described above), set to 5, which is used to obtain conservative estimates of the response and to avoid responders due to small standard deviations pre-stimulation.

An in-house python code was developed to filter out values with error code-signals before analysis (i.e. if the continuous HR monitoring is lost, as described by manufacturer), and to implement the formulas for HR analysis.

2.8. Statistics

Data are expressed as Mean $\pm$ SEM unless otherwise stated. One-way analysis of variance (ANOVA) with Dunnett's multiple comparison test, repeated measurements, was used for comparing frequencies.

2.9. Light propagation simulations with Monte Carlo

We used the Monte Carlo method to investigate light propagation in a model slice of mouse tissue, represented by a multilayered structure. The model represents tissue volume under the laser incidence and consists of three components: 0.5 mm skin, 2 mm fat, and 22.5 mm muscle (figure 4(A1)). Several optical parameters, such as thickness d, refractive index n, absorption coefficient μ_a, scattering coefficient μ_s, and g-factor, were assigned to each layer. Parameter values were adopted for 638 nm laser from [46, 59] and were summarized in supplementary table 1. After meshing the geometry with a step of 0.05 mm, 10^9 phonons were launched at the laser incidence point. Results were finalized with the convolution of absorption map for laser with beam parameters 1 mm half-width at half-maximum, and total power of 0.7 W. Monte-Carlo simulations were performed with the well-known software package CUDA MCML [60, 61].

2.10. Finite element analysis of mouse tissue heating by laser

Heating and heat dissipation was analyzed by using the finite element method. Three layered cubic model of a fraction of mouse tissue was used to investigate heat transfer during the VNS (figure 4(B1)). The thicknesses of skin, fat and muscle layers were the same as in the Monte Carlo simulation. All parameters are listed in supplementary table 2 and were adopted from [46] and references therein. Bioheat transfer was studied in the Pennes approximation [62] and captures the main features of living tissue, such as blood perfusion heat transfer, metabolical heating, and convection heat exchange

$$\rho C_p \frac{dT}{dt} + \nabla \cdot q = Q_{bio} + Q_{laser} \qquad (8)$$

$$q = -k\nabla T \qquad (9)$$

$$Q_{bio} = \rho_b C_{p,b} \omega_b (T_b - T) + Q_{met} \qquad (10)$$

$$Q_{laser} = Ae^{-\left(x^2/2w_1 - y^2/2w_1 - z^2/2w_2\right)} \qquad (11)$$

where ρ—density, Q_{met}—metabolic heating, C_p—heat capacity at constant pressure, q—heat flux, ω_b—blood perfusion, T_b—blood temperature, k—thermal conductivity, Q_{bio}—heat sources, which represent biological aspects of heat transfer.

A laser heat source Q_{laser} was adopted from previously calculated light absorption data by fitting absorption in each tissue layer with a Gaussian function with details and parameters listed in supplementary figure S4.

Simulations were conducted with COMSOL software package [57].

3. Results and discussion

3.1. A flexible stimulation array to improve electrode configurations

To study the stimulation efficacy of different microelectrode layouts and different stimulation parameters simultaneously, we developed a flexible, implantable stimulation array capable of closely enwrapping the vagus nerve (figures 1(A) and 2). The stimulation array was configured with eight larger (stimulation) and seven smaller (recording, not used in this study) contact surfaces (figure 2(A)). The electrode surfaces were coated with the conductive polymer PEDOT:PSS to improve the electrochemical impedance (electrochemical characterization shown in figure S1) and ensure that low voltages are maintained for the utilized stimulation currents [63–65]. The electrode dimensions were designed to fully wrap around the mouse vagus nerve with a diameter of ~180 μm [52]. The electrode array
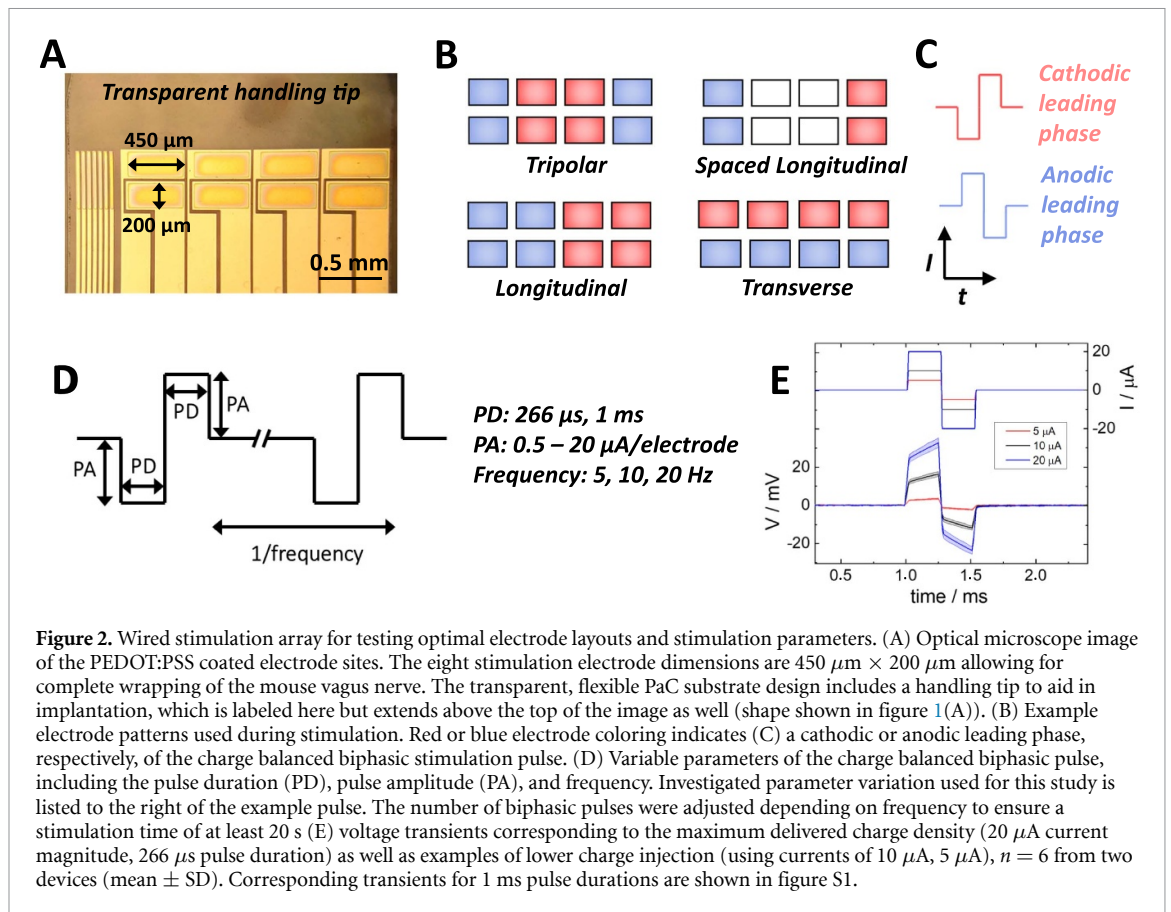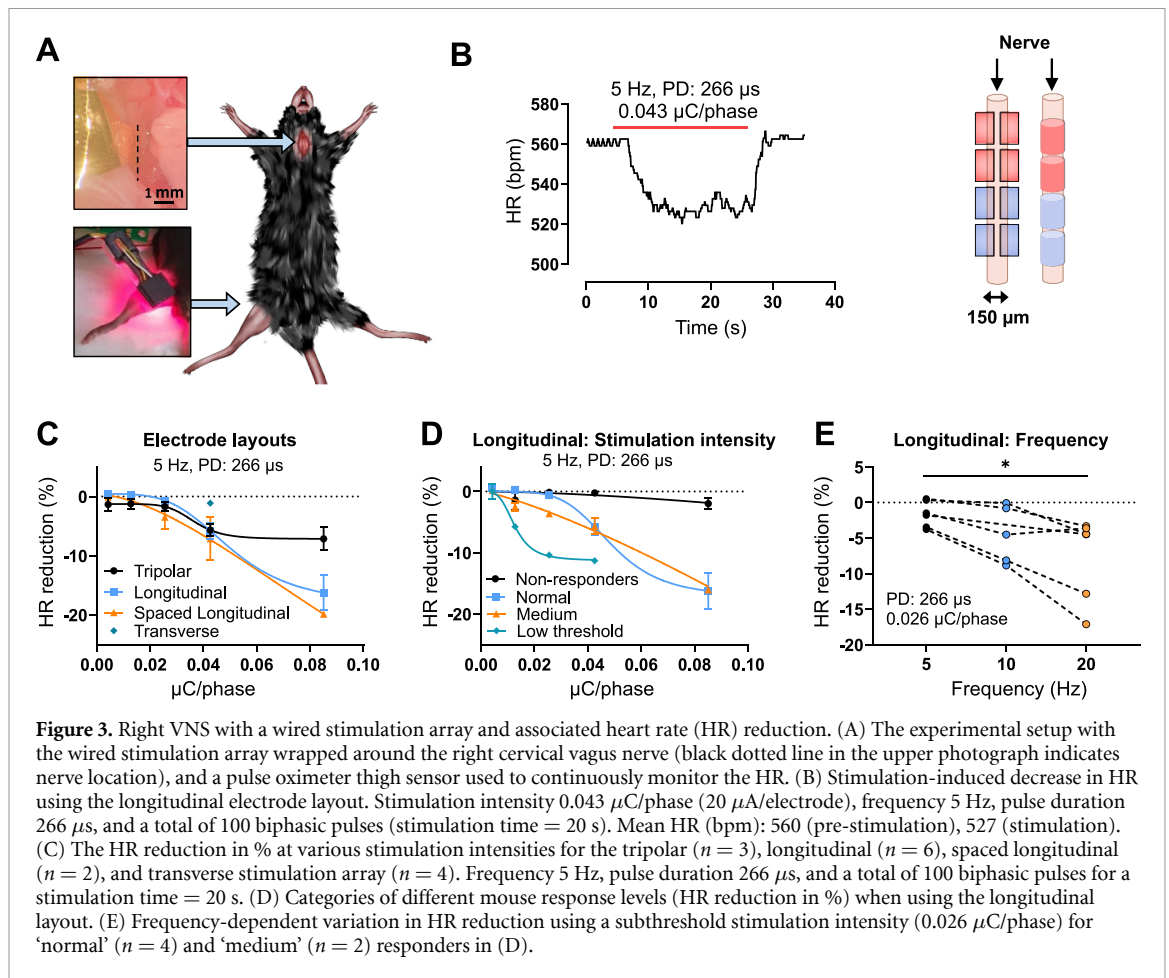
Figure 2. Wired stimulation array for testing optimal electrode layouts and stimulation parameters. (A) Optical microscope image of the PEDOT:PSS coated electrode sites. The eight stimulation electrode dimensions are 450 μm $\times$ 200 μm allowing for complete wrapping of the mouse vagus nerve. The transparent, flexible PaC substrate design includes a handling tip to aid in implantation, which is labeled here but extends above the top of the image as well (shape shown in figure 1(A)). (B) Example electrode patterns used during stimulation. Red or blue electrode coloring indicates (C) a cathodic or anodic leading phase, respectively, of the charge balanced biphasic stimulation pulse. (D) Variable parameters of the charge balanced biphasic pulse, including the pulse duration (PD), pulse amplitude (PA), and frequency. Investigated parameter variation used for this study is listed to the right of the example pulse. The number of biphasic pulses were adjusted depending on frequency to ensure a stimulation time of at least 20 s (E) voltage transients corresponding to the maximum delivered charge density (20 μA current magnitude, 266 μs pulse duration) as well as examples of lower charge injection (using currents of 10 μA, 5 μA), $n = 6$ from two devices (mean $\pm$ SD). Corresponding transients for 1 ms pulse durations are shown in figure S1.

arrangement permits a variety of electrical stimulation patterns, including grouping electrodes with cathodic or anodic leading phases first (figure 2(B)) to create bipolar and tripolar layouts with variable electrode spacings (figure 2(C), red or blue color coding indicates cathodic or anodic leading phase, respectively). These electrode patterns may be seen as providing the opportunity to mimic traditional stimulation electrodes, such as cuff electrodes but with a more conformal material system, as well as testing other geometric variations. Biphasic, charge-balanced stimulation pulses were used throughout the study, with current magnitude, frequency, pulse duration, and number of pulses independently definable for each electrode. Figure 2(D) shows these definable parameters with a cathodic leading pulse example, along with the various settings used in this study. All electrodes are referenced to an external ground wire. Voltage transients for the minimum and maximum charge delivered per electrode for our utilized parameters are shown in figure 2(E).

3.2. Optimal electrode layouts and stimulation parameters for activating the right vagus nerve in mice

In figure 3(A), the wired stimulation array is shown when wrapped around the right cervical vagus nerve. A pulse oximeter (MouseOx instrument, STARR Life Sciences) with a thigh sensor (also shown

in figure 3(A)) was used to continuously monitor the HR. Four different electrode patterns, readily adaptable to wireless photovoltaic device fabrication, were investigated using the wired stimulation array (figures 2(B) and 3(B)). The shown color coding of the electrodes indicates a cathodic leading pulse (red) or anodic leading pulse (blue). The protocol for our main methodical investigation of HR-reduction as a result of stimulation parameter and layout variation began with a frequency of 5 Hz, pulse duration of 266 μs, and the stimulation intensity was modulated by increasing the current amplitude (see figure 2(D)). In total 100 biphasic stimulation pulses were delivered, stimulating the nerve for 20 s, providing a stable reduced HR level for analysis (see example in figure 3(B)). The longitudinal and tripolar layout significantly reduced the HR by 5.8 $\pm$ 1.4 ($n = 6$) and 5.7 $\pm$ 1.1 ($n = 3$)%, respectively, when the stimulation intensity reached 0.043 μC/phase, while the transverse layout ($n = 4$) never elicited a response at this stimulation intensity even if the mouse responded well when stimulated with other electrode layouts (figure 3(C)). The spaced longitudinal layout performed similar to the longitudinal and tripolar layout for some mice ($n = 2$). However, for other cases we were not able to determine a proper stimulation intensity-response relationship. In these instances, the same stimulation intensity elicited very irregular HR reductions

Figure 3. Right VNS with a wired stimulation array and associated heart rate (HR) reduction. (A) The experimental setup with the wired stimulation array wrapped around the right cervical vagus nerve (black dotted line in the upper photograph indicates nerve location), and a pulse oximeter thigh sensor used to continuously monitor the HR. (B) Stimulation-induced decrease in HR using the longitudinal electrode layout. Stimulation intensity 0.043 μC/phase (20 μA/electrode), frequency 5 Hz, pulse duration 266 μs, and a total of 100 biphasic pulses (stimulation time = 20 s). Mean HR (bpm): 560 (pre-stimulation), 527 (stimulation). (C) The HR reduction in % at various stimulation intensities for the tripolar ($n = 3$), longitudinal ($n = 6$), spaced longitudinal ($n = 2$), and transverse stimulation array ($n = 4$). Frequency 5 Hz, pulse duration 266 μs, and a total of 100 biphasic pulses for a stimulation time = 20 s. (D) Categories of different mouse response levels (HR reduction in %) when using the longitudinal layout. (E) Frequency-dependent variation in HR reduction using a subthreshold stimulation intensity (0.026 μC/phase) for 'normal' ($n = 4$) and 'medium' ($n = 2$) responders in (D).

for the same mouse over time, from 3% to 30% reduction in HR, which was not observed for other electrode layouts. A possible explanation is that the spaced longitudinal layout, using only four stimulating electrodes, is more sensitive to proper placement than the longitudinal and tripolar layouts with eight stimulating electrodes. Based on our experimental observations, the longitudinal configuration using all eight electrodes resulted in clear and stable HR reduction throughout the experiments when stimulating the right cervical vagus nerve. In total, this longitudinal layout was investigated in 13 mice, in parallel to later testing the wireless photovoltaic devices. Figure 3(D) categorizes different levels of response for a specific set of parameters (5 Hz, PD: 266 μs, 100 biphasic pulses, at different stimulation intensities); two mice were non-responders (no response at $\geqslant 0.043$ μC/phase), six mice were normal responders (significant HR reduction at 0.043 μC/phase), three mice were medium responders (significant HR reduction at 0.026 μC/phase, or a significant HR reduction < 5% at 0.013 μC/phase), and two mice were 'low threshold' responders (significant HR reduction at <0.013 μC/phase, or a significant HR reduction >5% at 0.013 μC/phase). This grouping of response levels was determined empirically with the wired stimulation array and is important for wireless

photovoltaic device testing, discussed in the following next section. When increasing the frequency at a subthreshold stimulation intensity (0.026 μC/phase), the HR response increased (figure 3(E)). This variation with frequency is a known phenomenon [30], and was also tested with the wireless photovoltaic devices.

Taken together, it was demonstrated that the wired electrode array can be used to simultaneously test different stimulation parameters and electrode layouts. We initially focused on four different electrode patterns readily adaptable to the photovoltaic device fabrication. The most reliable and efficient HR reduction was seen with the longitudinal layout. Overall, we investigated the wired electrode array, and wireless photovoltaic stimulators in parallel in order to determine optimal stimulation parameters and device design for a strong physiological effect of VNS on HR.

3.3. Computer simulations

We utilized finite element modeling to help in understanding experiments in two respects: the first is optical power transfer through tissue, and the question of photothermal heating. The second is electric field distribution in the vagus nerve as a function of electrode geometry and injected current. Powering photovoltaic stimulation electrodes requires exposing
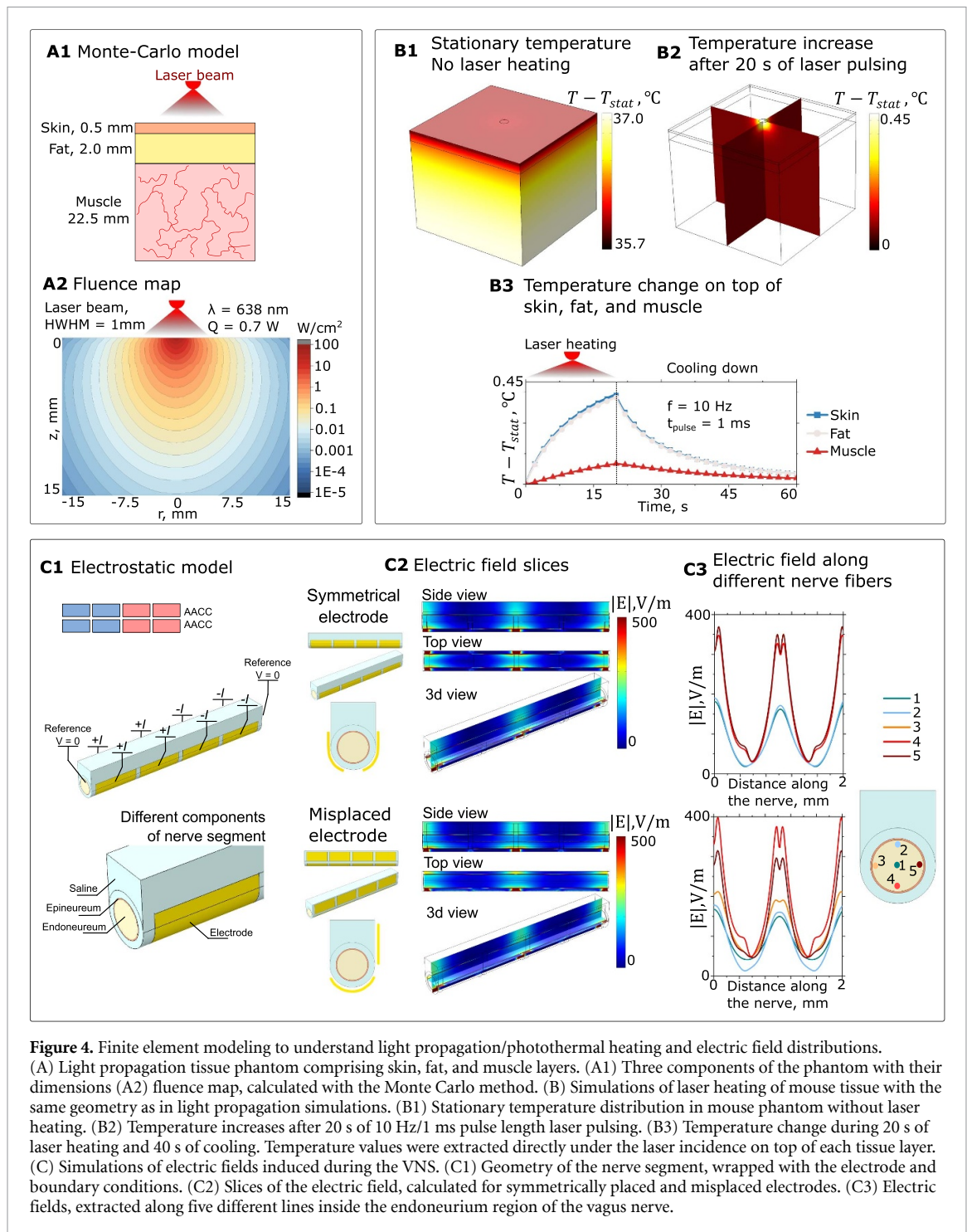
Figure 4. Finite element modeling to understand light propagation/photothermal heating and electric field distributions.
(A) Light propagation tissue phantom comprising skin, fat, and muscle layers. (A1) Three components of the phantom with their dimensions (A2) fluence map, calculated with the Monte Carlo method. (B) Simulations of laser heating of mouse tissue with the same geometry as in light propagation simulations. (B1) Stationary temperature distribution in mouse phantom without laser heating. (B2) Temperature increases after 20 s of 10 Hz/1 ms pulse length laser pulsing. (B3) Temperature change during 20 s of laser heating and 40 s of cooling. Temperature values were extracted directly under the laser incidence on top of each tissue layer. (C) Simulations of electric fields induced during the VNS. (C1) Geometry of the nerve segment, wrapped with the electrode and boundary conditions. (C2) Slices of the electric field, calculated for symmetrically placed and misplaced electrodes. (C3) Electric fields, extracted along five different lines inside the endoneurium region of the vagus nerve.

mouse tissue to red light with a wavelength of 638 nm, total maximum power of 0.7 W and half width half maximum of 1 mm. Light propagates through the tissue with intense scattering and resulting absorption profile. Even though laser power decays with propagation deeper into the tissue, it is sufficiently high for activation of photocapacitors at a distance of up to several mm deep [46]. We investigate light propagation in a fraction of a mouse tissue by using the Monte Carlo method. The geometry of the phantom consisted of skin with a thickness of 0.5 mm, 2 mm fat,

and a 22.5 mm muscle layer under it (figure 4(A1)). Simulations show that laser light can deeply propagate into tissue (figure 4(A2)). Of all laser power, 3% reflects from the skin boundary, 38% of light leaves the tissue after propagating inside, thus contributing to diffusive reflection, and 59% of the laser power absorbs inside the tissue. Among this absorbed fraction, 11.5% is absorbed by the skin layer, 28% by the fat layer and 19.4% is absorbed inside the muscle layer, which means that regarding the thickness of a fat layer, a sufficient amount of light propagates deep

into the mouse tissue and can power up an implant with tens of mW cm^{-2} of power at a depth of around 1 cm.

Absorbed laser also results in photothermal heating. Long-term laser exposure can potentially lead to tissue damage. To investigate this question, we use previously calculated light absorption data as a heat source to simulate biological heat transfer in mouse tissue near the laser incidence spot. Accounting for biological aspects of heat transfer such as blood perfusion and skin convection we calculated stationary temperature distribution inside tissue phantom before laser heating (figure 4(B1)), with temperature varying from 37 °C in the muscle domain to 35.7 °C on top of the mouse skin. After 20 s of laser pulsing (10 Hz and 1 ms pulse duration), the maximum temperature increase has reached 0.45 °C under the laser incidence (figure 4(B2)). In figure 4(B3) one can find accurate values of temperature increase on top of each tissue layer—skin, fat, and muscle. Because of the light scattering, skin and fat layers are heated at a similar temperature, while the muscle domain remains unchanged. During the next 40 s, heated regions were cooled down and temperature values returned to their normal values.

Finite element modeling was also used to understand the distribution of electric field around the nerve when considering different stimulation electrode layouts. Stimulation threshold variability when using VNS can arise due to the heterogenous organization of the axons in the nerve between subjects and species [50, 66–68], and thus also in relation to the electrode placement and pattern. To investigate if an electric field variability aids in explaining the biological variability observed with the longitudinal stimulation array above (figure 4(C)), we used a finite element method to simulate electric fields and potentials inside a 3D segment of the mouse vagus nerve wrapped in a longitudinal stimulation array. The system's geometry can be found in figure 4(C1) (see figure S2 for size details). The stimulated nerve segment was subjected to current pulses, analogous to those used in the experiments (figure 4(C), PD = 266 μs, PA = 20 μA/electrode, see section 2), and the electric fields inside the nerve were calculated at the end of each pulse phase.

The longitudinal stimulation array layout consists of eight electrodes, half of which have a cathodic-leading and half an anodic-leading phase (figure 4(C1)). Such a geometry creates a potential drop between electrodes with the opposite current magnitude in the pulse phases. The electric field is proportional to the voltage gradient and is especially pronounced in the areas between the electrode patches. On the other hand, dielectric and electron-transport properties of nerve tissue are highly inhomogeneous and anisotropic. The nerve conductivity has been reported as 6–7 times larger in

an axial direction than in the radial direction [58]. In contrast, the conductivity in the outer nerve shell is small to prevent signal distortion (see table S3 for details). These factors create a unique distribution of electric fields inside the nerve that would not be expected from considering an isotropic medium of a cylindrical geometry.

An example of |E| mapping can be found in figure 4(C2), which is depicted on the front, side, and 3d view slices. The electric field has increased values near the middle of the electrode (transition between cathodic and anodic electrodes) and on the sides of the nerve segment due to a current dissipation towards the reference. The shape of the electrode array is the primary source of inhomogeneity of the electric field (figure 4(C2)). Different electrode configurations will lead to different electric fields. The electrode placement also plays an essential role in forming the resulting electric field. We simulate the same electrode configuration at two different electrode placements (figure 4(C2)). The first one is symmetric placement, or what can be called 'perfect placement'. In such geometry, the electrode array is located as close as possible to the nerve, with only a saline layer separating them. The second configuration represents severely misplaced and asymmetrical electrodes. Half of the asymmetrical electrode is positioned under the nerve and half is shifted on the side with a large amount of saline buffer. For better understanding, we extracted normalized electric field values along the five lines inside endoneurium, depicted in figure 4(C3). Electric field values dramatically change along the nerve, with values from 20 to 380 V m^{-1} with the maximum values located under the interelectrode areas, where the voltage difference is the largest. The electric field varies not just in a longitudinal direction but also in a radial. |E| near the surface of the nerve is larger than in the middle, thus making inner axons less susceptible to stimulation than outer axons. This large variety in electric field inside of the nerve may account for some of the observed variability of animal response: based on the anatomical position of the critical axons in question, there are large differences in the E-field. Moreover, non-ideal placement of the electrode introduces even more variety into electric field distribution along the nerve. Even though the misplaced electrode still creates large electric fields, a large part of the nerve is subjected to even smaller |E| than in the case of a symmetrically placed electrode.

In summary, the simulations highlight that variation in electrode placement and randomness in the positioning of the axons can cause a difference in the resulting electric field even for the same longitudinal stimulation array, despite the small diameter of the vagus nerve in mice. This shows the magnitude to which electrode placement may affect the threshold variability for different animals above, emphasizing
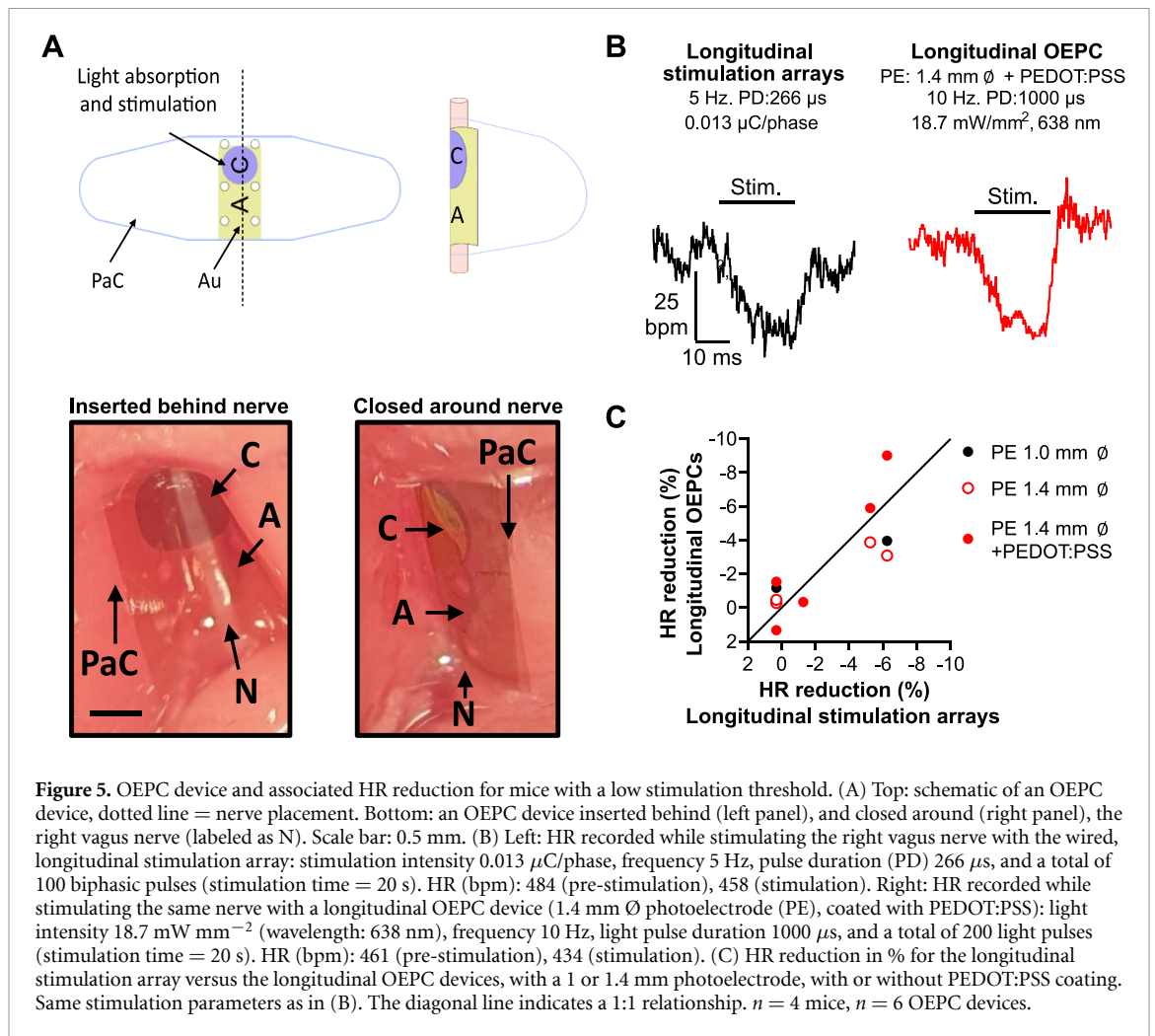
Figure 5. OEPC device and associated HR reduction for mice with a low stimulation threshold. (A) Top: schematic of an OEPC device, dotted line = nerve placement. Bottom: an OEPC device inserted behind (left panel), and closed around (right panel), the right vagus nerve (labeled as N). Scale bar: 0.5 mm. (B) Left: HR recorded while stimulating the right vagus nerve with the wired, longitudinal stimulation array: stimulation intensity 0.013 μC/phase, frequency 5 Hz, pulse duration (PD) 266 μs, and a total of 100 biphasic pulses (stimulation time = 20 s). HR (bpm): 484 (pre-stimulation), 458 (stimulation). Right: HR recorded while stimulating the same nerve with a longitudinal OEPC device (1.4 mm $\emptyset$ photoelectrode (PE), coated with PEDOT:PSS): light intensity 18.7 mW mm^{-2} (wavelength: 638 nm), frequency 10 Hz, light pulse duration 1000 μs, and a total of 200 light pulses (stimulation time = 20 s). HR (bpm): 461 (pre-stimulation), 434 (stimulation). (C) HR reduction in % for the longitudinal stimulation array versus the longitudinal OEPC devices, with a 1 or 1.4 mm photoelectrode, with or without PEDOT:PSS coating. Same stimulation parameters as in (B). The diagonal line indicates a 1:1 relationship. $n = 4$ mice, $n = 6$ OEPC devices.

the importance of fabricating carefully-fitted, conformable ultrathin electrodes.

3.4. OEPC devices effectively reduce the HR for mice with a low stimulation threshold

OEPC devices, which convert tissue-penetrating deep-red light to electrical signals, have recently been shown to wirelessly activate large single cells [43, 69], explanted retinas [45], somatosensory cortex in mice [44], and the rat sciatic nerve for over 100 d *in vivo* [46]. We therefore wanted to explore if the OEPC devices also could be used as minimalistic electrodes for stimulating the right vagus nerve of mice. In light of the findings for effective stimulation array layouts, OEPC devices with a 1 or 1.4 mm ($\emptyset$ in diameter) photoelectrode pixel on a 2.43 mm × 1.2 mm or 2 mm semi-transparent Au return electrode were manufactured on an ultra-thin, biocompatible PaC substrate in a longitudinal configuration (figures 1(B) and 5(A)). The photoelectrode ('C', figure 5(A)) consists of a PN heterojunction made of organic semi-conducting materials (metal-free phthalocyanine (H$_2$Pc), p-type and *N,N'*-dimethylperylene-3,4:9,10-tetracarboxylic diimide (PTCDI), n-type), and is responsible for photogeneration of charge. Upon

illumination with deep-red light (638 nm), a biphasic stimulation pulse is elicited as negative charges accumulate at the electrolytic interface of the n-type layer and positive charges flow to the return electrode [43, 46]. The magnitude of stimulation is related to the light intensity, light pulse length, and the size of the photoelectrode that is used [45, 46]. To enhance the performance of some OEPC devices, a coating of the conducting polymer PEDOT:PSS on top of the PN layer was also used. This coating decreases the interfacial impedance, increases the charge storage capacity, and in turn increases the maximal transient voltage responsible for stimulating the nerve by a factor of 2–3 [44, 69].

First, we implanted the wired array around the right cervical vagus nerve and assessed the charge needed to generate a significant HR reduction, using a frequency of 5 Hz, and a pulse width of 266 μs as described above (figure 3(C)). Thereafter, the stimulation array was removed from the vagus nerve and the OEPC device was implanted around the same nerve with the photoelectrode and return electrode adjacent to the epineurium. The device was fixed in place simply through the adhesion of the PaC surfaces with one another (figure 5(A)), sufficient

for short-term experiments. Subsequently, the OEPC device was exposed to pulsed deep-red illumination, using a 638 nm laser diode, with no tissue obscuring the light path. Previously we have shown 500–1000 μs long light-pulses are needed for an OEPC device with a 1.4 mm Ø sized photoelectrode to robustly stimulate the rat sciatic nerve and evoke muscle responses [46]. Here, using the wired stimulation array, we have also shown that higher stimulation frequencies can be used to increase the effect on the HR (figure 3(E)). With this information, initial optimal light parameters were determined to be 1000 μs light pulse duration, delivered at a frequency of 10 Hz (in total 200 light pulses), using the maximum light power (18.7 mW mm^{-2}, 638 nm). Upon illumination of the OEPC devices with these parameters, a reduction in HR (<10%) was observed, most pronounced for OEPC devices with a 1.4 mm Ø photoelectrode coated with PEDOT:PSS. Based on previous studies of OEPC devices, this size of PN is expected to deliver roughly 0.015–0.030 μC for a 1 ms light pulse of this light intensity. Consistent with this charge value, the OEPC-induced HR reduction was only seen for mice with a low stimulation threshold (figure 5(B,C)), determined using the wired longitudinal stimulation array (figures 3(C) and (D)). Given that the light intensity for these experiments was already at the maximum level, effective use of OEPC devices for long-term stimulation of the small diameter vagus nerve in mice was considered to be unlikely, in particular when placed underneath the tissue. We therefore moved to exploring the use of photovoltaic flags, which allow for higher levels of photogenerated charge.
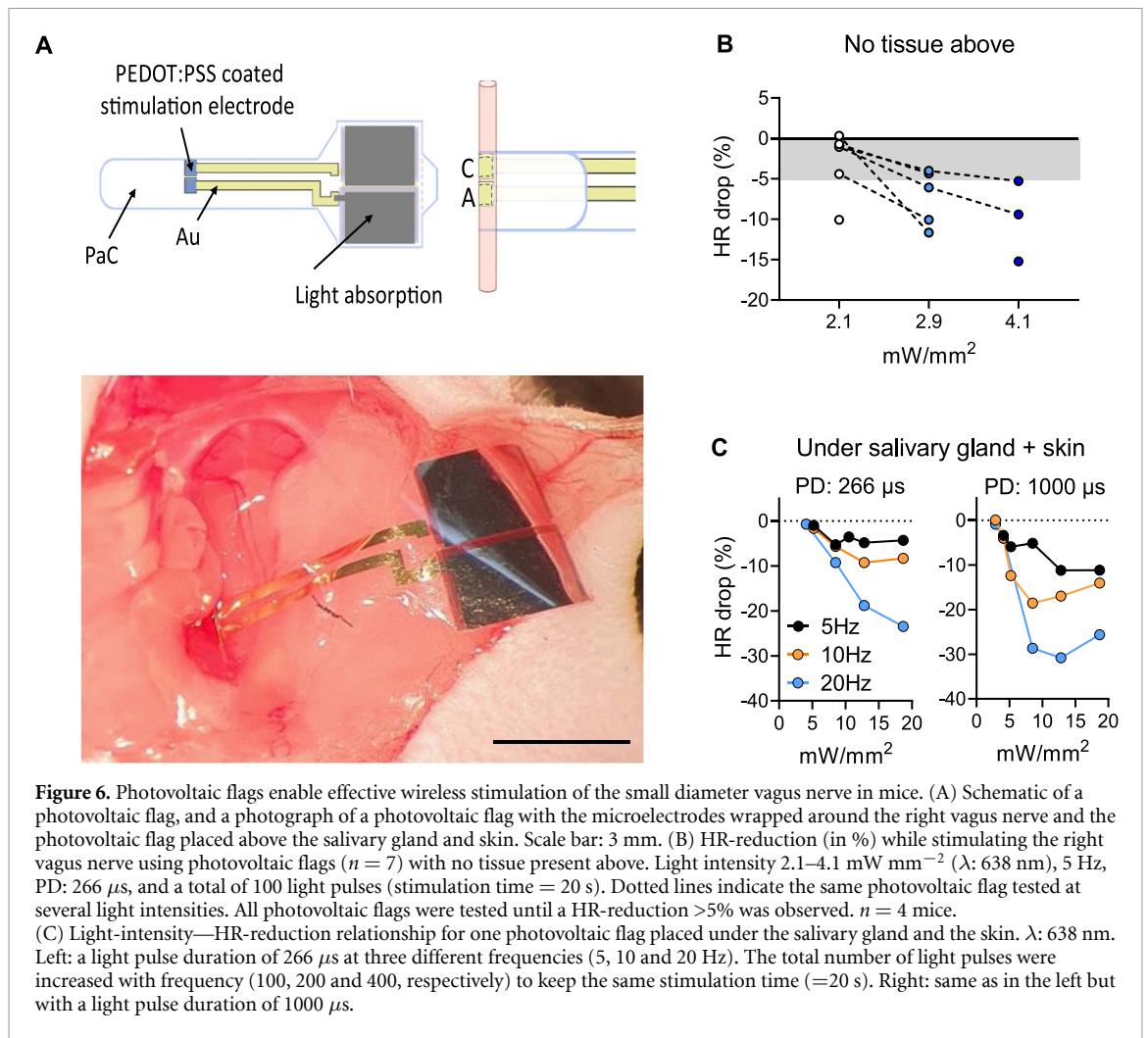
3.5. Photovoltaic flags enable efficient wireless stimulation of the vagus nerve in mice

The photoelectrode of OEPCs is responsible for both light absorption and nerve stimulation (figure 1(B)), which allows a minimalistic device design. This can, however, be a limitation when stimulating small diameter nerves or when targeted biological structures lie relatively deep in the tissue. The photoelectrode should have a large enough area to generate sufficient charge during light absorption. However, if the area is too large, parts of the photoelectrode will not be in direct contact with the nerve, thus decreasing stimulation efficiency. Therefore, we tested whether a photovoltaic flag (figure 1(C)) could be more efficient when stimulating a small diameter nerve, such as the vagus nerve in mice. Photovoltaic flags also enable wireless stimulation (as OEPC devices), however the larger photovoltaic driver consisting of the same PN junction (flag) can generate more charge during light absorption, and at the same time the charge can be better concentrated at the nerve interface through the use of PEDOT:PSS coated microelectrodes, fabricated to fit the small size of the nerve (figures 1(C) and 6(A)). We fabricated the

photovoltaic flag with two PN junctions connected in series with titanium metal as a top contact layer, using procedures reported recently for photovoltaic-driven ion pumps [70]. The two PN junctions are interconnected to PEDOT:PSS coated stimulation electrodes using PaC-encapsulated gold leads. We characterized the photocharging currents by electrolytically contacting each microelectrode and measuring according to the electrophotoresponse method established in previous work [71]. These measured charge densities delivered photovoltaically are in-line (5–55 μC cm^{-2}) with what is passed through the wired array to evoke HR reduction (figure S3).

As before, we first determined the charge per phase needed to induce a significant HR-reduction using the wired longitudinal stimulation array for each mouse. Thereafter, we removed the array and placed a wireless photovoltaic flag around the same nerve. Figure 6(A) shows the placement of a photovoltaic flag with the microelectrodes wrapped around the nerve, and the photovoltaic driver placed above the salivary gland and the skin. We expected that the photovoltaic flags would be capable of inducing a larger HR-reduction as compared to the OEPC devices. Therefore, the initial utilized frequency was 5 Hz, with a light pulse duration of 266 μs, and in total 100 light pulses (total stimulation time = 20 s) from a low light intensity (2.1 mW mm^{-2}, 638 nm) which was increased (~1 mW mm^{-2} steps) until a clear HR reduction >5% was seen. All photovoltaic flags, tested on mice with a medium or normal stimulation-intensity response (determined with the wired stimulation array, see figure 3), significantly reduced the HR > 5% at lower light intensities (2–4 mW mm^{-2}, figure 6(B)), which was clearly an improvement in performance compared to the OEPC devices. The photovoltaic flag which had the smallest HR-reduction at 4.1 mW mm^{-2} was utilized for further tests to allow exploration of other parameters (e.g. frequency, pulse duration, light intensity) without inducing HR reductions that were too large (e.g. repeatedly causing oxygen saturation to drop below 60%–70%, which in our experiments occurred when the HR reduction was around 25%–30%). This device was also placed under the salivary gland and the skin (figure 6(C)), increasing the light intensity needed to induce a significant HR-reduction by around 50% (⩾8.5 mW mm^{-2} figure 6(C), left). Increasing the frequency did not lower the light intensity needed, but it increased the stimulation-induced HR-reduction (figure 6(C), left). At the maximum light intensity (18.7 mW mm^{-2}), at 20 Hz, the photovoltaic flag lowered the HR with 23% (figure 6(C), left). The light-intensity could however be lowered to 4–5 mW mm^{-2} by increasing the light pulse length to 1000 μs (figure 6(C), right).

This part of our study demonstrates that the photovoltaic flags were capable of wirelessly stimulating the small diameter vagus nerve in all

Figure 6. Photovoltaic flags enable effective wireless stimulation of the small diameter vagus nerve in mice. (A) Schematic of a photovoltaic flag, and a photograph of a photovoltaic flag with the microelectrodes wrapped around the right vagus nerve and the photovoltaic flag placed above the salivary gland and skin. Scale bar: 3 mm. (B) HR-reduction (in %) while stimulating the right vagus nerve using photovoltaic flags ($n = 7$) with no tissue present above. Light intensity 2.1–4.1 mW mm^{-2} (λ: 638 nm), 5 Hz, PD: 266 μs, and a total of 100 light pulses (stimulation time $= 20$ s). Dotted lines indicate the same photovoltaic flag tested at several light intensities. All photovoltaic flags were tested until a HR-reduction >5% was observed. $n = 4$ mice.
(C) Light-intensity—HR-reduction relationship for one photovoltaic flag placed under the salivary gland and the skin. λ: 638 nm. Left: a light pulse duration of 266 μs at three different frequencies (5, 10 and 20 Hz). The total number of light pulses were increased with frequency (100, 200 and 400, respectively) to keep the same stimulation time ($=20$ s). Right: same as in the left but with a light pulse duration of 1000 μs.

mice despite the threshold variability. Importantly, the feasibility of wireless electrical stimulation of the vagus nerve with 'flag' placement under the salivary gland and skin was also clearly demonstrated. This could in the future enable wireless long-term functional mapping of neural reflexes in freely moving mice.

4. Conclusion

Well-established genetic mouse models are available for the study of key elements of disease pathogenesis in mice, but long-term functional studies of VNS have not been possible because of the limitations of available nerve stimulation technologies [7]. The mechanistic understanding of chronic VNS has therefore been limited. This makes studying VNS in the context of diseases that develop over time, such as chronic inflammatory conditions, very difficult. To tackle this problem, the bioelectronics field must develop flexible, minimalistic device designs together with wireless powering for small-animal experiments. However, a technical challenge for wirelessly powered devices is achieving or maintaining high performance when placed within the body.

Here, we report the development of a thin, flexible, wired stimulation array, used to help optimize the design of wireless photovoltaic-based stimulators. The wired array allows simultaneous control over both electrode layouts and stimulation parameters (figures 1(A) and 2). This stimulation array was used to determine the charge threshold for activating the right cervical vagus nerve in mice evidenced by reduced HR. The electrode layouts explored were chosen since they readily could be adopted in the design and fabrication of the wireless devices, which transduce tissue-penetrating deep-red light into electrical signals. The wired stimulation array demonstrated that the charge threshold needed to activate right vagus nerve was dependent on the utilized electrode layout (figure 3(C)). However, there was also a threshold variability between different animals, even when the same electrode layout was used (figure 3(D)). This highlights the importance of the possibility to modify electrode layout and stimulation parameters without the need of changing devices. To aid in the understanding of variability between animals, we have employed computer simulations for the most stable electrode layout, the longitudinal layout. These simulations show that the axon/bundle

arrangement inside the peripheral nerve can result in relatively large differences in electric field, despite the fact that the nerve is of relatively small diameter. Electric field varies by up to 2.5 times in radial direction (within the nerve slice), and orders of magnitude between different positions along the whole nerve (both in axial and radial directions). The sharp differences in radial electric field especially could explain some of the variability observed here between animals, which was also reported in other studies.

After exploring different electrode layouts and stimulation parameters with the wired array, we designed ultrathin and flexible OEPC devices in the longitudinal layout (figures 1(B) and 4). The aim was to investigate if they could be used to wirelessly stimulate the vagus nerve in mice, and possibly enable future long-term chronic VNS studies in small laboratory animals. However, our findings show that OEPC-mediated VNS only can be achieved for mice with a very low charge threshold (determined by using the wired stimulation array), and when there is no tissue above the light absorbing photoelectrode. Little room exists for further optimizing the OEPC performance as the small diameter nerve limits the size of the photoelectrode. Our findings suggest the use of a photovoltaic flag, which has a larger photovoltaic driver (for more efficient charge generation), and microelectrodes fabricated to fit the small diameter vagus nerve (that can concentrate the generated charge to the nerve) (figure 1(C)). This provides a fully implantable, wireless solution while maintaining the flexible, minimally invasive nature of the overall device. Indeed, the photovoltaic flags were capable of wirelessly stimulating the small diameter vagus nerve in all mice despite the charge threshold variability between animals. Importantly, the photovoltaic flags were also capable of electrically activating the nerve when the optical path was obstructed by placing the device under the salivary gland and skin. Direct optical, photovoltaic-mediated stimulation may be a minimalistic alternative for neurostimulation for animal experiments that can be easier to implement than other wireless modalities. Overall, our results contribute to the notion that red light is a viable technique for transcutaneous wireless power transfer, where relatively high amounts of power density (tens to hundreds of $mW\,cm^{-2}$) can be transferred through an intact tissue interface with minimal photothermal heating. While this study has been limited to understanding the variation among animals and finding optimal device parameters, the results open the door for an assortment of long-term testing opportunities using the photovoltaic flag. The main considerations that are needed to achieve this prospect include a locking mechanism to maintain a conformal interface between the electrode sites and the vagus nerve (similar to the *in vivo* sciatic nerve solution [46]) as well as fixation for the photovoltaic flag. It is expected that employing these adaptations will allow for investigation of use in different disease models for weeks up to 6 months based on previous stability results when using an analogous material system [46]. For longer (6+ months–years) the stability will need to be further investigated and failure mechanisms addressed.

Data availability statement

All data that support the findings of this study are included within the article (and any supplementary files).

Author contributions

M J D, M S E, and M J contributed equally to this work. M J D, M S E, M J, P S O and E D G conceived the ideas and experiments. A S C, M J D, M S E, and M J performed acute experiments. M S E, M J D, M J and V D carried out characterization and analysis of devices and obtained data. M J D designed and fabricated wired grid electrodes. M J designed and fabricated the optoelectronic stimulators. I S performed computational simulations. G A and H H developed code for automatic analysis of heart rate changes. M J D, M S E, A S C, P S O, and E D G wrote the manuscript with input from all other authors.

Conflict of interest

P S O is a shareholder of Emune AB. The authors declare no other conflicts of interest.

Ethical statement

The animal studies were approved by the Stockholm Regional Board for Animal Ethics protocols N104/16 and 20818-2020 (Stockholm, Sweden).

ORCID iDs

Marie Jakešová ⬩ https://orcid.org/0000-0002-8702-2303
Ihor Sahalianov ⬩ https://orcid.org/0000-0002-0609-471X
Peder S Olofsson ⬩ https://orcid.org/0000-0003-3473-5948
Eric Daniel Głowacki ⬩ https://orcid.org/0000-0002-0280-8017

References

[1] Bonaz B, Sinniger V and Pellissier S 2019 Vagus nerve stimulation at the interface of brain–gut interactions *Cold Spring Harb. Perspect. Med.* **9** a034199

[2] Capilupi M J, Kerath S M and Becker L B 2020 Vagus nerve stimulation and the cardiovascular system *Cold Spring Harb. Perspect. Med.* **10** a034173

[3] Olofsson P S and Bouton C 2019 Bioelectronic medicine: an unexpected path to new therapies *J. Intern. Med.* **286** 237–9

[4] Tracey K J 2002 The inflammatory reflex *Nature* **420** 853–9

[5] Caravaca A S, Centa M, Gallina A L, Tarnawski L and Olofsson P S 2020 Neural reflex control of vascular inflammation *Bioelectron. Med.* **6** 3

[6] Caravaca A S, Gallina A L, Tarnawski L, Tracey K J, Pavlov V A, Levine Y A and Olofsson P S 2019 An effective method for acute vagus nerve stimulation in experimental inflammation *Front. Neurosci.* **13** 877

[7] Mughrabi I T *et al* 2021 Development and characterization of a chronic implant mouse model for vagus nerve stimulation *eLife* **10** e61270

[8] Dali M, William L, Tigra W, Taillades H, Rossel O, Azevedo C and Guiraud D 2019 Relevance of selective neural stimulation with a multicontact cuff electrode using multicriteria analysis *PLoS One* **14** e0219079

[9] Datta-Chaudhuri T 2021 Closed-loop neuromodulation will increase the utility of mouse models in bioelectronic medicine *Bioelectron. Med.* **7** 10

[10] Noller C M, Levine Y A, Urakov T M, Aronson J P and Nash M S 2019 Vagus nerve stimulation in rodent models: an overview of technical considerations *Front. Neurosci.* **13** 911

[11] Rosenthal N and Brown S 2007 The mouse ascending: perspectives for human-disease models *Nat. Cell Biol.* **9** 993–9

[12] Penry J K and Dean J C 1990 Prevention of intractable partial seizures by intermittent vagal stimulation in humans: preliminary results *Epilepsia* **31** S40–3

[13] Ben-Menachem E 2002 Vagus-nerve stimulation for the treatment of epilepsy *Lancet Neurol.* **1** 477–82

[14] O'Reardon J P, Cristancho P and Peshek A D 2006 Vagus nerve stimulation (VNS) and treatment of depression: to the brainstem and beyond *Psychiatry* **3** 54–63

[15] Nesbitt A D, Marin J C A, Tompkins E, Ruttledge M H and Goadsby P J 2015 Initial use of a novel noninvasive vagus nerve stimulator for cluster headache treatment *Neurology* **84** 1249–53

[16] Bonaz B *et al* 2016 Chronic vagus nerve stimulation in Crohn's disease: a 6-month follow-up pilot study *Neurogastroenterol. Motil.* **28** 948–53

[17] Genovese M C, Gaylis N B, Sikes D, Kivitz A, Horowitz D L, Peterfy C, Glass E V, Levine Y A and Chernoff D 2020 Safety and efficacy of neurostimulation with a miniaturised vagus nerve stimulation device in patients with multidrug-refractory rheumatoid arthritis: a two-stage multicentre, randomised pilot study *Lancet Rheumatol.* **2** e527–38

[18] Koopman F A *et al* 2016 Vagus nerve stimulation inhibits cytokine production and attenuates disease severity in rheumatoid arthritis *Proc. Natl Acad. Sci. USA* **113** 8284–9

[19] Pavlov V A, Chavan S S and Tracey K J 2020 Bioelectronic medicine: from preclinical studies on the inflammatory reflex to new approaches in disease diagnosis and treatment *Cold Spring Harb. Perspect. Med.* **10** a034140

[20] Cimpianu C-L, Strube W, Falkai P, Palm U and Hasan A 2017 Vagus nerve stimulation in psychiatry: a systematic review of the available evidence *J. Neural Transm.* **124** 145–58

[21] Dawson J *et al* 2016 Safety, feasibility, and efficacy of vagus nerve stimulation paired with upper-limb rehabilitation after ischemic stroke *Stroke* **47** 143–50

[22] Yamakawa K, Rajendran P S, Takamiya T, Yagishita D, So E L, Mahajan A, Shivkumar K and Vaseghi M 2015 Vagal nerve stimulation activates vagal afferent fibers that reduce cardiac efferent parasympathetic effects *Am. J. Physiol. Heart. Circ. Physiol.* **309** H1579–90

[23] Levine Y A, Koopman F, Faltys M, Caravaca A, Bendele A, Zitnik R, Vervoordeldonk M J and Tak P P 2014 Neurostimulation of the cholinergic anti-inflammatory pathway ameliorates disease in rat collagen-induced arthritis *PLoS One* **9** e104530

[24] Bansal V, Ryu S Y, Lopez N, Allexan S, Krzyzaniak M, Eliceiri B, Baird A and Coimbra R 2012 Vagal stimulation modulates inflammation through a ghrelin mediated mechanism in traumatic brain injury *Inflammation* **35** 214–20

[25] Huffman W J, Subramaniyan S, Rodriguiz R M, Wetsel W C, Grill W M and Terrando N 2019 Modulation of neuroinflammation and memory dysfunction using percutaneous vagus nerve stimulation in mice *Brain Stimul.* **12** 19–29

[26] Huston J M *et al* 2006 Splenectomy inactivates the cholinergic antiinflammatory pathway during lethal endotoxemia and polymicrobial sepsis *J. Exp. Med.* **203** 1623–8

[27] Inoue T, Abe C, Sung S-S J, Moscalu S, Jankowski J, Huang L, Ye H, Rosin D L, Guyenet P G and Okusa M D 2016 Vagus nerve stimulation mediates protection from kidney ischemia-reperfusion injury through α7nAChR+ splenocytes *J. Clin. Invest.* **126** 1939–52

[28] Le Maître E, Revathikumar P, Estelius J and Lampa J 2017 Increased recovery time and decreased LPS administration to study the vagus nerve stimulation mechanisms in limited inflammatory responses *J. Vis. Exp.* **121** 54890

[29] Meneses G *et al* 2016 Electric stimulation of the vagus nerve reduced mouse neuroinflammation induced by lipopolysaccharide *J. Inflamm.* **13** 33

[30] Rajendran P S *et al* 2019 Identification of peripheral neural circuits that regulate heart rate using optogenetic and viral vector strategies *Nat. Commun.* **10** 1944

[31] Tsaava T *et al* 2020 Specific vagus nerve stimulation parameters alter serum cytokine levels in the absence of inflammation *Bioelectron. Med.* **6** 8

[32] Wang H *et al* 2003 Nicotinic acetylcholine receptor alpha7 subunit is an essential regulator of inflammation *Nature* **421** 384–8

[33] Wright J P *et al* 2022 A fully implantable wireless bidirectional neuromodulation system for mice *Biosens. Bioelectron.* **200** 113886

[34] Caravaca A S *et al* 2017 A novel flexible cuff-like microelectrode for dual purpose, acute and chronic electrical interfacing with the mouse cervical vagus nerve *J. Neural Eng.* **14** 066005

[35] Falcone J D, Liu T, Goldman L, David D P, Bouton C E, Straka M and Sohal H S 2020 A novel microwire interface for small diameter peripheral nerves in a chronic, awake murine model *J. Neural Eng.* **17** 046003

[36] Giagka V and Serdijn W A 2018 Realizing flexible bioelectronic medicines for accessing the peripheral nerves—technology considerations *Bioelectron. Med.* **4** 8

[37] Khodagholy D, Gelinas J N, Thesen T, Doyle W, Devinsky O, Malliaras G G and Buzsáki G 2015 NeuroGrid: recording action potentials from the surface of the brain *Nat. Neurosci.* **18** 310–5

[38] Lienemann S, Zötterman J, Farnebo S and Tybrandt K 2021 Stretchable gold nanowire-based cuff electrodes for low-voltage peripheral nerve stimulation *J. Neural Eng.* **18** 045007

[39] Singer A *et al* 2020 Magnetoelectric materials for miniature, wireless neural stimulation at therapeutic frequencies *Neuron* **107** 631–43.e5

[40] Piech D K, Johnson B C, Shen K, Ghanbari M M, Li K Y, Neely R M, Kay J E, Carmena J M, Maharbiz M M and Muller R 2020 A wireless millimetre-scale implantable neural stimulator with ultrasonically powered bidirectional communication *Nat. Biomed. Eng.* **4** 207–22

[41] Cotero V *et al* 2019 Noninvasive sub-organ ultrasound stimulation for targeted neuromodulation *Nat. Commun.* **10** 952

[42] Jiang Y *et al* 2018 Rational design of silicon structures for optically controlled multiscale biointerfaces *Nat. Biomed. Eng.* **2** 508–21

[43] Jakešová M *et al* 2019 Optoelectronic control of single cells using organic photocapacitors *Sci. Adv.* **5** eaav5265

[44] Missey F, Botzanowski B, Migliaccio L, Acerbo E, Głowacki E D and Williamson A 2021 Organic electrolytic photocapacitors for stimulation of the mouse somatosensory cortex *J. Neural Eng.* **18** 066016

[45] Rand D, Jakešová M, Lubin G, Vēbraitė I, David-Pur M, Ðerek V, Cramer T, Sariciftci N S, Hanein Y and Głowacki E D 2018 Direct electrical neurostimulation with organic pigment photocapacitors *Adv. Mater.* **30** e1707292

[46] Silverå Ejneby M *et al* 2022 Chronic electrical stimulation of peripheral nerves via deep-red light transduced by an implanted organic photocapacitor *Nat. Biomed. Eng.* **6** 741–53

[47] Vasudevan S, Patel K and Welle C 2017 Rodent model for assessing the long term safety and performance of peripheral nerve recording electrodes *J. Neural Eng.* **14** 016008

[48] Lee B, Koripalli M K, Jia Y, Acosta J, Sendi M S E, Choi Y and Ghovanloo M 2018 An implantable peripheral nerve recording and stimulation system for experiments on freely moving animal subjects *Sci. Rep.* **8** 6115

[49] Shafer B, Welle C and Vasudevan S 2019 A rat model for assessing the long-term safety and performance of peripheral nerve electrode arrays *J. Neurosci. Methods* **328** 108437

[50] Bucksot J E, Wells A J, Rahebi K C, Sivaji V, Romero-Ortega M, Kilgard M P, Ii R L R and Hays S A 2019 Flat electrode contacts for vagus nerve stimulation *PLoS One* **14** e0215191

[51] Pelot N A, Goldhagen G B, Cariello J E, Musselman E D, Clissold K A, Ezzell J A and Grill W M 2020 Quantified morphology of the cervical and subdiaphragmatic vagus nerves of human, pig, and rat *Front. Neurosci.* **14** 1148

[52] Stakenborg N, Gomez-Pinilla P J, Verlinden T J M, Wolthuis A M, D'Hoore A, Farré R, Herijgers P, Matteoli G and Boeckxstaens G E 2020 Comparison between the cervical and abdominal vagus nerves in mice, pigs, and humans *Neurogastroenterol. Motil.* **32** e13889

[53] Ahmed U, Chang Y C, Cracchiolo M, Lopez M F, Tomaio J N, Datta-Chaudhuri T, Zanos T P, Rieth L, Al-Abed Y and Zanos S 2020 Anodal block permits directional vagus nerve stimulation *Sci. Rep.* **10** 9221

[54] Ottaviani M M, Vallone F, Micera S and Recchia F A 2022 Closed-loop vagus nerve stimulation for the treatment of cardiovascular diseases: state of the art and future directions *Front. Cardiovasc. Med.* **9** 866957

[55] Qing K Y, Wasilczuk K M, Ward M P, Phillips E H, Vlachos P P, Goergen C J and Irazoqui P P 2018 B fibers are the best predictors of cardiac activity during vagus nerve stimulation *Bioelectron. Med.* **4** 5

[56] Donahue M J, Kaszas A, Turi G F, Rózsa B, Slézia A, Vanzetta I, Katona G, Bernard C, Malliaras G G and Williamson A 2018 Multimodal characterization of neural networks using highly transparent electrode arrays *eNeuro* **5** ENEURO.0187–18.2018

[57] COMSOL Multiphysics® version 5.6 (Stockholm: COMSOL AB) (available at: www.comsol.com)

[58] Romeni S, Valle G, Mazzoni A and Micera S 2020 Tutorial: a computational framework for the design and optimization of peripheral neural interfaces *Nat. Protocols* **15** 3129–53

[59] Bashkatov A N, Genina E A and Tuchin V V 2011 Optical properties of skin, subcutaneous, and muscle tissues: a review *J. Innov. Opt. Health Sci.* **04** 9–38

[60] Wang L, Jacques S L and Zheng L 1995 MCML–Monte Carlo modeling of light transport in multi-layered tissues *Comput. Methods Programs Biomed.* **47** 131–46

[61] Alerstam E, Svensson T and Andersson-Engels S 2008 Parallel computing with graphics processing units for high-speed Monte Carlo simulation of photon migration *J. Biomed. Opt.* **13** 060504

[62] Pennes H H 1948 Analysis of tissue and arterial blood temperatures in the resting human forearm *J. Appl. Physiol.* **1** 93–122

[63] Boehler C, Aqrawe Z and Asplund M 2019 Applications of PEDOT in bioelectronic medicine *Bioelectron. Med.* **2** 89–99

[64] Donahue M J, Sanchez-Sanchez A, Inal S, Qu J, Owens R M, Mecerreyes D, Malliaras G G and Martin D C 2020 Tailoring PEDOT properties for applications in bioelectronics *Mater. Sci. Eng. R* **140** 100546

[65] Wilks S J, Richardson-Burns S M, Hendricks J L, Martin D C and Otto K J 2009 Poly(3,4-ethylenedioxythiophene) as a micro-neural interface material for electrostimulation *Front. Neuroeng.* **2** 7

[66] Butler A G, O'Callaghan E L, Allen A M and McDougall S J 2021 Use of a physiological reflex to standardize vagal nerve stimulation intensity improves data reproducibility in a memory extinction assay *Brain Stimul.* **14** 450–9

[67] Frei M G and Osorio I 2001 Left vagus nerve stimulation with the neurocybernetic prosthesis has complex effects on heart rate and on its variability in humans *Epilepsia* **42** 1007–16

[68] Settell M L *et al* 2020 Functional vagotopy in the cervical vagus nerve of the domestic pig: implications for the study of vagus nerve stimulation *J. Neural Eng.* **17** 026022

[69] Silverå Ejneby M, Migliaccio L, Gicevičius M, Ðerek V, Jakešová M, Elinder F and Głowacki E D 2020 Extracellular photovoltage clamp using conducting polymer-modified organic photocapacitors *Adv. Mater. Technol.* **5** 1900860

[70] Jakešová M, Sjöström T A, Ðerek V, Poxson D, Berggren M, Głowacki E D and Simon D T 2019 Wireless organic electronic ion pumps driven by photovoltaics *npj Flex. Electron.* **3** 1–6

[71] Ðerek V, Rand D, Migliaccio L, Hanein Y and Głowacki E D 2020 Untangling photofaradaic and photocapacitive effects in organic optoelectronic stimulation devices *Front. Bioeng. Biotechnol.* **8** 284